

Thermodynamic sampling of materials using neutral-atom quantum computers

Bruno Camino^{1*}, Mao Lin^{2*}, John Buckeridge³ and Scott M. Woodley⁴

¹*Chemistry Department, University College London, 20 Gordon St, London, WC1H 0AJ, United Kingdom.

²Amazon Braket, Seattle, 98170, WA, United States.

³School of Engineering, London South Bank University, 103 Borough Rd, London, SE10 AA, United Kingdom.

*Corresponding author(s). E-mail(s): b.camino@ucl.ac.uk;
maolinml@amazon.com;

Contributing authors: j.buckeridge@lsbu.ac.uk; scott.woodley@ucl.ac.uk;

Abstract

Neutral-atom quantum hardware has emerged as a promising platform for programmable many-body physics. In this work, we develop and validate a practical framework for extracting thermodynamic properties of materials using such hardware. As a test case, we consider nitrogen-doped graphene. Starting from Density Functional Theory (DFT) formation energies, we map the material energetics onto a Rydberg-atom Hamiltonian suitable for quantum annealing by fitting an on-site term and distance-dependent pair interactions. The Hamiltonian derived from DFT cannot be implemented directly on current QuEra devices, as the largest energy scale accessible on the hardware is two orders of magnitude smaller than the target two-body interaction in the material. To overcome this limitation, we introduce a rescaling strategy based on a single parameter, α_v , which ensures that the Boltzmann weights sampled by the hardware correspond exactly to those of the material at an effective temperature $T' = \alpha_v T$, where T is the device sampling temperature. This rescaling also establishes a direct correspondence between the global laser detuning Δ_g and the grand-canonical chemical potential $\Delta\mu$. We validate the method on a 28-site graphene nanoflake using exhaustive enumeration, and on a larger 78-site system where Monte Carlo sampling confirms preferential sampling of low-energy configurations.

Keywords: Thermodynamic sampling, Neutral-atom quantum computing, Quantum annealing, Rydberg Hamiltonian, Boltzmann sampling

1 Introduction

The majority of technologically relevant materials exhibit some degree of disorder, such as vacancies, interstitial species, amorphous regions, solid solutions, or substitutional alloys. To predict their properties reliably, it is necessary to employ not only accurate energetic models but also representations capable of capturing the effects of configurational complexity. Here, we are motivated by the general problem of modelling solid solutions, *i.e.*, predicting the atomic order or disorder for a known lattice where multiple atomic species can occupy equivalent lattice sites. The result will depend on the temperature and the relative chemical potential between the competing species.

Employing a unit cell with periodic boundary conditions significantly reduces the number of variables required to simulate the atomistic structure of a perfectly ordered crystal. For solid solutions, this concept is commonly extended through the use of supercells, which are constructed by repeating the primitive or unit cell of the underlying lattice to form a larger simulation cell containing many more lattice sites. As the supercell size increases, both the computational cost of evaluating the energy of each configuration and the number of distinct atomic configurations grow rapidly, rendering exhaustive enumeration computationally prohibitive even for relatively simple energy models. While real materials are not constrained by supercell size, any computational results must nevertheless be assessed for convergence with respect to this approximation.

Several classical approaches have been developed to find low-energy configurations or solid solutions, including Monte Carlo sampling, simulated annealing, and genetic algorithms, among others [1–4]. In recent years, quantum technologies—and quantum annealing in particular—have attracted increasing attention as an alternative approach [5–7]. In our previous work [8], we demonstrated how the investigation of solid solutions can be formulated as a Quadratic Unconstrained Binary Optimisation (QUBO) [9, 10] model and implemented on D-Wave quantum annealers [11]. We also showed how such devices can be used to recover thermodynamic properties of materials within the grand canonical ensemble.

In the present work, we take nitrogen-doped graphene as a test case to illustrate how a configurational optimisation problem can be mapped onto a Rydberg Hamiltonian [12–14] and implemented on neutral-atom quantum hardware, as realised on the Aquila QuEra device [15, 16]. Neutral-atom platforms offer several notable advantages: they operate at room temperature without the need for cryogenic cooling, allow for programmable atom positions and interaction ranges, and can function in both continuous-time (annealing) and digital modes. Recent experiments have demonstrated the possibility of dynamically moving atoms within the array, opening perspectives for highly reconfigurable quantum simulations [14, 17]. Here, however, we focus exclusively on the annealing mode of operation.

The energy model for the material is mapped to the Rydberg Hamiltonian, which depends on only two tunable parameters: an on-site term corresponding to a controllable laser detuning, and a pair term representing the Rydberg-state interaction $C_6/R_{i,j}^6$, where C_6 is the interaction parameter between the atoms in the hardware and $R_{i,j}$ is the distance between sites i and j on the device. This mapping introduces substantial challenges beyond those encountered in Ref. [8]. The currently available hardware used in this work - the QuEra Aquila device - allows only two-dimensional atomic arrangements, motivating the choice of graphene as a model system for this proof of concept. Even within two dimensions, atom placement is subject to geometric constraints, such as minimum distances between sites and between adjacent rows. Furthermore, the energy window accessible through laser detuning is significantly narrower than the range of formation energies typically encountered in materials systems, requiring additional theoretical treatment.

The main objective of this work is to develop, in a proof-of-concept framework, a theoretical and computational mapping between materials science models and the Rydberg Hamiltonian, while assigning a clear thermodynamic meaning to the hardware control parameters. This allows the distributions generated by the device to be interpreted as equilibrium ensembles of the corresponding material. The key result of this study is the derivation of a rescaling factor, α_v , which uniformly rescales both the on-site and pair contributions in the energy model. We show that the Boltzmann distribution sampled by the annealer can be interpreted as that of the physical system at an elevated effective temperature $T' = \alpha_v T$, where T is the effective annealing temperature. In addition, we demonstrate that the laser detuning Δ_g acquires a direct grand-canonical interpretation as a chemical potential difference $\Delta\mu$, establishing a one-to-one correspondence between device control parameters and thermodynamic variables.

We validate the proposed mapping by studying the nitrogen distribution in a 28-site graphene nanoflake, comparing the quantum hardware results with exhaustive classical enumeration across detuning (chemical potential) values. We then extend the analysis to a 78-site graphene nanoflake, for which full enumeration is computationally unfeasible, and benchmark the device output against unbiased Monte Carlo simulations. Finally, we demonstrate that varying the interatomic separation allows one to sample effective distributions corresponding to different temperatures, confirming the thermodynamic consistency of the proposed scaling.

Overall, this work provides a proof-of-concept demonstration of an exact mapping between Density Functional Theory (DFT) [18, 19] derived formation energies and a Rydberg Hamiltonian, along with a rescaling procedure that enables the implementation of realistic material models on available quantum hardware. Although currently limited to two-dimensional systems, the method is readily applicable to three-dimensional materials as hardware capabilities evolve [20]. Because neutral atoms are also promising candidates for digital quantum computing, the approach developed here represents a potential building block for future hybrid workflows that combine continuous-time annealing and digital quantum algorithms for materials discovery.

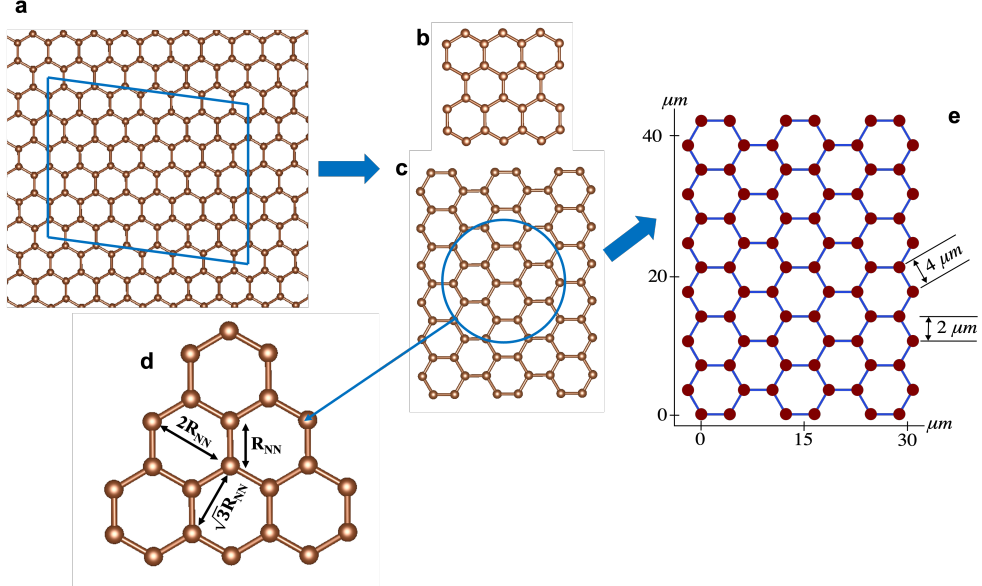


Fig. 1 Structure of the graphene model used in this study and its mapping to the quantum hardware. **a** Periodic structure employed for the CRYSTAL DFT calculations. **b** Graphene nanoflake with 28 atoms used in the exhaustive search simulations (Section 2.4). **c** Graphene nanoflake with 78 atoms used in the Monte Carlo simulations (Section 2.5). **d** Zoom-in illustrating the distance between lattice sites in terms of the distance between nearest neighbours R_{NN} . **e** Mapping of the structure in panel **c** onto neutral atoms using $R_{NN} = 4.0 \mu\text{m}$.

2 Results

2.1 Constructing the Rydberg Hamiltonian from DFT Data

We build the energy model used in the annealing from periodic Density Functional Theory (DFT) calculations. The computational details of these calculations can be found in Section 4.1. The 78-atom unit cell used in the DFT calculations is depicted in blue in panel **a** of Fig. 1. We build the training and test sets comprising 2145 and 2184 structures, respectively, each containing between one and ten nitrogen atoms, corresponding to a maximum nitrogen concentration of 12.8%. Using the symmetry considerations described in the Methods section, the structures in both the training and test sets are reduced to only 28 symmetry-independent configurations (SIC) in each set. Their energies are calculated using the PBE [21] functional and a p-*p*VTZ [22] basis set as implemented in the CRYSTAL23 code [23]. To be able to compare the energy of structures characterised by different nitrogen concentrations, we calculate the formation energy as:

$$\Delta E_k^f = E_k - \sum_{\chi^i} N_k^{\chi^i} E_{\chi^i}, \quad (1)$$

where E_k is the total relaxed DFT energy per simulation cell for configuration k ; $N_k^{\chi^i}$ is the number of χ^i atoms in configuration k ; and E_{χ^i} is the DFT energy of species χ^i in its reference state. We used N_2 for the nitrogen energy reference and the energy of a carbon atom in the pristine graphene structure as a reference for carbon. This ensures that the ΔE_k^f for pristine graphene is zero and the energy of all doped structures is positive.

In a system of Rydberg atoms, the time evolution is governed by the following Hamiltonian [16]:

$$H(t) = \sum_{i=1}^N H_{\text{drive},i}(t) + \sum_{i=1}^{N-1} \sum_{j>i}^N H_{\text{vdW},i,j}, \quad (2)$$

where

$$H_{\text{drive},i}(t) = \frac{\Omega(t)}{2} \left(e^{i\phi(t)} |g_i\rangle\langle r_i| + e^{-i\phi(t)} |r_i\rangle\langle g_i| \right) - \Delta_g(t) n_i, \quad (3)$$

and

$$H_{\text{vdW},i,j} = V_{i,j} n_i n_j = \frac{C_6}{R_{i,j}^6} n_i n_j. \quad (4)$$

The term $H_{\text{drive},i}(t)$ denotes a global Rabi drive that addresses the atoms simultaneously and uniformly, where $\Omega(t)$, $\phi(t)$ and $\Delta_g(t)$ denote the amplitude, phase and detuning of the driving field. Here $|g_i\rangle$ and $|r_i\rangle$ denote the ground and Rydberg states of the i -th atom and $n_i \equiv |r_i\rangle\langle r_i|$ is the occupation number operator. At the beginning of the annealing protocol, all atoms are prepared in their ground states, which yields the many-body ground state of $H(t)$ for $\Omega(t) = 0$, $\phi(t) = 0$, and $\Delta_g(t) < 0$. During the evolution process, we keep $\phi(t) = 0$ and ramp $\Omega(t)$ (with a trapezoidal profile) while increasing $\Delta_g(t)$, driving the atoms into superposition of the ground and Rydberg states. At the end of the annealing process, we turn $\Omega(t)$ down to zero and set the global detuning to a final value Δ_g , then perform a projective measurement, yielding the Rydberg occupation of each atom: $n_i = 1$ if the i -th atom is in the Rydberg state otherwise $n_i = 0$. The term $H_{\text{vdW},i,j}$ describes the two-body interaction between a pair of atoms, which depends on their occupation numbers n_i , separation $R_{i,j}$, and a hardware-specific constant C_6 (which is set to 5.42×10^{-24} rad m⁶/s in this work). We note that the interatomic separations $R_{i,j}$ are fixed throughout the annealing process.

The tunable parameters that allow the Rydberg Hamiltonian to encode a given problem are therefore the final global detuning Δ_g and the interatomic separations $R_{i,j}$. The formation energies of the structures in the training set are mapped to the Rydberg Hamiltonian by minimising the following linear regression:

$$\min_{\{V^{\text{DFT}}, V_{i,j}^{\text{DFT}}\}} \sum_{k=1}^{N_{\text{train}}} \left[\Delta E_k^f - \left(\sum_i V^{\text{DFT}} n_i^k + \sum_{ij} V_{i,j}^{\text{DFT}} n_i^k n_j^k \right) \right]^2, \quad (5)$$

where N_{train} is the number of structures in the training set, ΔE_k^f is the formation energy for structure k as defined in Eq. 1, V^{DFT} is the on-site energy, which is the same for all sites, and $V_{i,j}^{\text{DFT}}$ is the two-body potential between sites i and j . The variables n_i^k are the components of the site-occupation vector \mathbf{n}^k for configuration k .

Here, $n_i^k = 1$ implies that site i is occupied by a nitrogen atom, and $n_i^k = 0$ a carbon atom. By writing the two-body potential explicitly, we obtain:

$$\min_{\{V^{\text{DFT}}, R_{i,j}^{\text{DFT}}\}} \sum_{k=1}^{N_{\text{train}}} \left(\Delta E_k^f - \left(\sum_i V^{\text{DFT}} n_i^k + \sum_{ij} \frac{C_6}{(R_{i,j}^{\text{DFT}})^6} n_i^k n_j^k \right) \right)^2, \quad (6)$$

where the two-body potential has been explicitly expressed through its dependence on the distance between sites $R_{i,j}^{\text{DFT}}$.

We can simplify Eq. 6 further by taking into consideration two factors. First, in the unit cell displayed in panel **a** of Fig. 1, all sites are equivalent. This means that the interaction between neighbouring sites $V_{i,j}$ is the same for all couples i and j . Therefore, we can define a single distance between neighbouring sites R_{NN} that applies to all couples i and j of nearest neighbours. The distances between next nearest neighbours can be obtained by using simple geometrical considerations as shown in the panel **d** of Fig. 1. Secondly, because $H_{\text{vdW},i,j}$ scales as $R_{i,j}^{-6}$, the mapping can be truncated at the fourth nearest neighbours, for which the interaction energy has already decayed to $\frac{1}{343} V_{\text{NN}}$ (the fourth nearest neighbour in a hexagonal lattice is at a distance of $\sqrt{7} R_{\text{NN}}$). Therefore, Eq. 6 becomes:

$$\begin{aligned} \min_{\{V^{\text{DFT}}, R_{\text{NN}}^{\text{DFT}}\}} \sum_{k=1}^{N_{\text{train}}} & \left(\Delta E_k^f - \left(\sum_i V^{\text{DFT}} n_i^k + \right. \right. \\ & \sum_{ij \in \text{NN}} \frac{C_6}{(R_{\text{NN}}^{\text{DFT}})^6} n_i^k n_j^k + \sum_{ij \in \text{NNN}} \frac{C_6}{(\sqrt{3} R_{\text{NN}}^{\text{DFT}})^6} n_i^k n_j^k + \\ & \left. \left. \sum_{ij \in \text{3NN}} \frac{C_6}{(2 R_{\text{NN}}^{\text{DFT}})^6} n_i^k n_j^k + \sum_{ij \in \text{4NN}} \frac{C_6}{(\sqrt{7} R_{\text{NN}}^{\text{DFT}})^6} n_i^k n_j^k \right) \right)^2, \end{aligned} \quad (7)$$

where the sums were limited to the fourth nearest neighbours (4NN). From Eq. 7 we obtain the V^{DFT} and $R_{\text{NN}}^{\text{DFT}}$ that will be used in the mapping to the quantum annealer.

Using Eq. 7, as implemented in [24] we obtain $V^{\text{DFT}} = 3.613 \times 10^{-4}$ eV and $R_{\text{NN}}^{\text{DFT}} = 1.6122 \mu\text{m}$. The model yields a correlation coefficient of $R = 0.9473$ on the training set, a mean squared error of 9.84×10^{-8} eV on the test set, and a Spearman's rank correlation coefficient of $\rho = 0.976$.

2.2 Setting the Composition through Detuning and Chemical Potential

When computing the formation energies ΔE_k^f from Eq. 1, pure graphene has $\Delta E_k^f = 0$ and all structures containing nitrogen atoms have $\Delta E_k^f > 0$. As quantum annealing typically finds the ground state solution, using the V^{DFT} and $R_{\text{NN}}^{\text{DFT}}$ values derived from Eq. 7 would result in identifying only the trivial solution consisting entirely of carbon atoms.

In our previous work [8], we mapped this class of problems onto QUBO models that were solved on D-Wave superconducting qubit quantum annealers and demonstrated that the outcome can be tuned toward a targeted composition by introducing a penalty on the on-site term of the QUBO expression. There, we further established the connection between this linear bias and the chemical potentials of the species in reservoirs in equilibrium with the material. To make this correspondence explicit, we introduce the grand-canonical formation energies as

$$\Delta\tilde{E}_k^f = \Delta E_k^f + \sum_{\chi^i} N_k^{\chi^i} \mu_{\chi^i}, \quad (8)$$

where ΔE_k^f is the canonical (fixed-composition) formation energy defined in Eq. 1, and $N_k^{\chi^i}$ and μ_{χ^i} denote, respectively, the number of atoms of species χ^i in configuration k and the corresponding chemical potential.

We define the chemical potential difference $\Delta\mu = \mu_N - \mu_C$ and write $\mu_N = \mu_C + \Delta\mu$, which for our chosen system gives

$$\Delta\tilde{E}_k^f = \Delta E_k^f + (N_k^C + N_k^N) \mu_C + N_k^N \Delta\mu. \quad (9)$$

Since we want $\Delta\tilde{E}_k^f = \Delta E_k^f$ when there are no nitrogen atoms available, we set $\mu_C = 0$, yielding

$$\Delta\tilde{E}_k^f = \Delta E_k^f + N_k^N \Delta\mu. \quad (10)$$

In the following sections, we use this form, in which the thermodynamics is fully controlled by the single parameter $\Delta\mu$.

A key consequence of this expression is that the chemical potential term adds a contribution that is linear in the number of nitrogen atoms N_k^N . In our encoding, nitrogen corresponds to $n_i = 1$ in the binary configuration returned by the quantum annealer. Therefore, introducing $\Delta\mu$ does not require refitting the parameters V^{DFT} and $R_{\text{NN}}^{\text{DFT}}$ obtained from Eq. 7. Instead, the chemical potential can be incorporated directly into the mapping as a shift of the on-site term:

$$\Delta\tilde{E}_k^f \approx \sum_i (V^{\text{DFT}} + \Delta\mu) n_i^k + \sum_{ij} \frac{C_6}{(R_{i,j}^{\text{DFT}})^6} n_i^k n_j^k, \quad (11)$$

where \approx indicates that this expression represents the optimal Rydberg-Hamiltonian approximation to the DFT formation energies achievable under the hardware constraints.

By comparing Eqs. 2 and 11, we find that the detuning parameter Δ_g in the quantum annealer corresponds to the term $(V^{\text{DFT}} + \Delta\mu)$ in our energy model. This correspondence forms the basis for the subsequent analysis, establishing a direct physical link between the thermodynamic control of chemical potential in the grand canonical ensemble and the tunable laser detuning Δ_g in the quantum hardware.

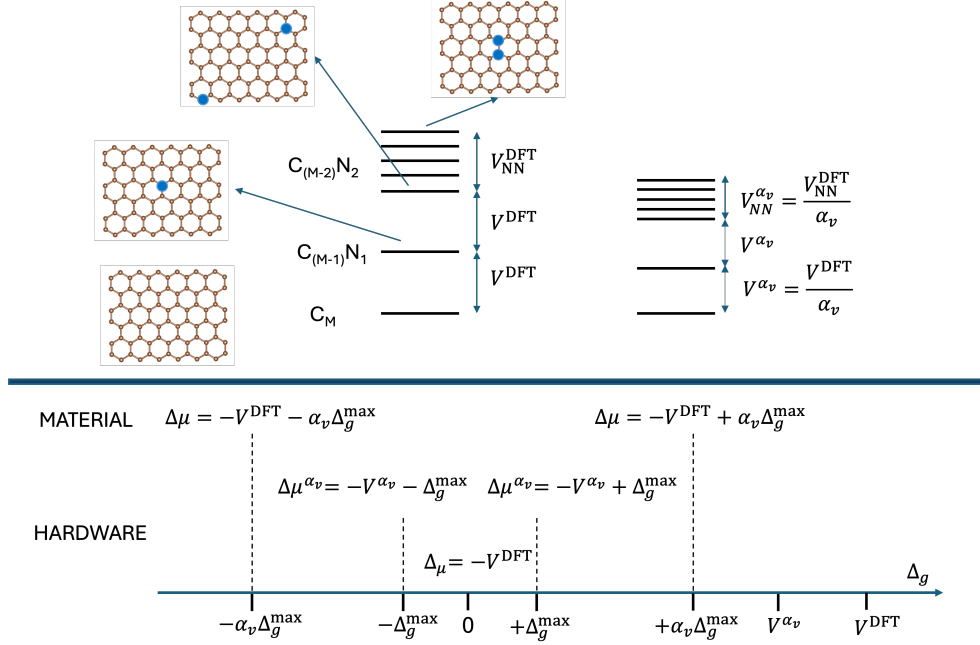


Fig. 2 Effect of scaling on the energy levels in the material and the hardware. **Top left:** energy levels of pure graphene (C_M) and graphene doped with one ($C_{(M-1)}N_1$) or two ($C_{(M-2)}N_2$) nitrogen atoms. V^{DFT} denotes the nitrogen on-site energy, and V_{NN}^{DFT} the two-body potential between neighbouring sites. **Top right:** α_v is the scaling factor used to map the DFT energies onto the hardware, subject to its constraints. $V_{NN}^{\alpha_v}$ is the scaled two-body potential between neighbouring sites, and V^{α_v} is the nitrogen on-site energy scaled consistently. **Bottom:** visual comparison (not to scale) of the energy levels with and without scaling in the material and the hardware. The term $\pm \Delta_g^{\text{max}}$ represents the global detuning range of the annealer. $\Delta\mu$ is the chemical potential range explored in terms of the DFT energy levels of the material, while $\Delta\mu^{\alpha_v}$ is the corresponding range scaled by α_v .

2.3 Implementing the Mapping within Hardware Constraints

When mapping the problem to a set of Rydberg atoms, as implemented in the QuEra Aquila device using the experimental setup, we need to take into account the following constraints:

- the maximum number of atoms is 256
- the maximum size of the atomic arrangement is $128\mu\text{m} \times 75\mu\text{m}$ (this is available in the tall geometry setup, the default is $76\mu\text{m} \times 75\mu\text{m}$)
- the range of global detuning Δ_g is $[-\Delta_g^{\text{max}}, \Delta_g^{\text{max}}]$ where $\Delta_g^{\text{max}} = 8.227649 \times 10^{-8}\text{eV}$
- the minimum distance allowed between two atoms is $R_{NN}^{\text{min}} = 4\mu\text{m}$
- the minimum distance allowed between two rows of atoms is $2\mu\text{m}$ (this is available in the tight geometry setup, the default is $4\mu\text{m}$)

The latter two constraints are depicted in panel e of Fig 1.

Specifically, due to constraints on the accessible global detuning range and the minimum allowed interatomic spacing, we cannot directly realise on this hardware the

DFT-derived parameters V^{DFT} ($3.614 \times 10^{-4} \text{ eV} \approx 237 \times \Delta_g^{\text{max}}$) and $R_{\text{NN}}^{\text{DFT}}$ ($1.6122 \mu\text{m} \approx 0.4 \times R_{\text{NN}}^{\text{min}}$). To address this mismatch, we develop and apply a systematic rescaling procedure that maps the DFT parameters to experimentally feasible values. This procedure is essential for modelling realistic atomic systems and constitutes a central contribution of this work. To illustrate the rescaling procedure, we begin with the energy levels of the nitrogen-doped graphene system, shown in Fig. 2. The top-left panel presents the progression of energy levels from pure graphene to configurations containing two nitrogen atoms. The term V^{DFT} represents the on-site energy associated with introducing a single nitrogen atom into the structure. To simplify the derivation of the equations needed for rescaling the energies, we assume here that all sites are equivalent, so that all configurations with just one carbon atom replaced with one nitrogen atom are degenerate. For structures containing two nitrogen atoms separated by more than four neighbours, we assume negligible interaction between nitrogen atoms, so the total energy of the structures is simply $2V^{\text{DFT}}$. In contrast, when the two nitrogen atoms occupy nearest-neighbour sites, the total energy becomes $2V^{\text{DFT}} + V_{\text{NN}}^{\text{DFT}}$, where

$$V_{\text{NN}}^{\text{DFT}} \equiv \frac{C_6}{(R_{\text{NN}}^{\text{DFT}})^6} \quad (12)$$

is the two-body interaction energy between neighbouring sites as derived from Eq. 5. Therefore, the energy separation between the highest and lowest-energy two-nitrogen configurations is $V_{\text{NN}}^{\text{DFT}}$. The energies discussed so far are those obtained by fitting the DFT results to the Rydberg Hamiltonian, *i.e.*, solving Eq. 7. However, the values of $V_{\text{NN}}^{\text{DFT}}$ lie beyond the hardware capabilities. In particular, the largest achievable two-body interaction between two nearest-neighbour atoms is

$$V_{\text{NN}}^{\alpha_v} \equiv \frac{C_6}{(R_{\text{NN}}^{\text{min}})^6}, \quad (13)$$

which is smaller than the DFT nearest-neighbour interaction $V_{\text{NN}}^{\text{DFT}}$ because $R_{\text{NN}}^{\text{DFT}} < R_{\text{NN}}^{\text{min}}$. To overcome this limitation, we introduce a rescaling factor

$$\alpha_v \equiv \frac{V_{\text{NN}}^{\text{DFT}}}{V_{\text{NN}}^{\alpha_v}} = \left(\frac{R_{\text{NN}}^{\text{min}}}{R_{\text{NN}}^{\text{DFT}}} \right)^6 \approx 236.69. \quad (14)$$

With this choice, reproducing the energy spectrum of the nitrogen-doped graphene system reduces to rescaling the Rydberg-atom energies by α_v . For consistency, we also rescale the on-site energy according to

$$V^{\alpha_v} \equiv \frac{V^{\text{DFT}}}{\alpha_v}. \quad (15)$$

We emphasise that introducing V^{α_v} is not enforced by the hardware capability, unlike $V_{\text{NN}}^{\alpha_v}$. Rather, its introduction enforces a uniform rescaling of the Hamiltonian, ensuring that the Boltzmann distribution generated by the hardware corresponds to that of the

original (unscaled) system, but at a higher effective temperature. In the following, we show how this correspondence can be derived exactly.

First, we consider the partition function in the grand canonical ensemble for the nitrogen-doped graphene:

$$\Xi = \sum_{k=0}^{N_n} M_k \exp \frac{-\Delta \tilde{E}_k^f}{k_B T} = \sum_{k=0}^{N_n} M_k \exp \frac{-(\Delta E_k^f + N_k^N \Delta \mu)}{k_B T}, \quad (16)$$

where T is the effective temperature to be determined (see Sec. 2.4) and all the other quantities have been defined above. To derive the grand canonical partition function Ξ under the hardware constraints, we begin by rescaling the exponent in Eq. 16 by α_v :

$$\Xi(T, \Delta\mu, \alpha_v) = \sum_{k=0}^{N_n} M_k \exp \left(\frac{-\Delta E_k^f - N_k^N \Delta \mu}{k_B T \alpha_v} \right) \quad (17a)$$

$$= \sum_{k=0}^{N_n} M_k \exp \left[\frac{-1}{k_B T} \left(\frac{\sum_i (V^{\text{DFT}} + \Delta\mu) n_i^k + \sum_{ij} V_{i,j}^{\text{DFT}} n_i^k n_j^k}{\alpha_v} \right) \right] \quad (17b)$$

$$= \sum_{k=0}^{N_n} M_k \exp \left[\frac{-1}{k_B T} \left(\sum_i \frac{(V^{\text{DFT}} + \Delta\mu)}{\alpha_v} n_i^k + \sum_{ij} \frac{C_6}{(R_{i,j}^{\text{min}})^6} n_i^k n_j^k \right) \right] \quad (17c)$$

$$= \sum_{k=0}^{N_n} M_k \exp \left[\frac{-1}{k_B T} \left(-\sum_i \Delta_g n_i^k + \sum_{ij} \frac{C_6}{(R_{i,j}^{\text{min}})^6} n_i^k n_j^k \right) \right], \quad (17d)$$

where we have used Eq. 5 in the derivation. As explained above, $V_{\text{NN}}^{\text{DFT}}/\alpha_v$ is the largest achievable two-body interaction when the nearest-neighbour sites are separated by $R_{\text{NN}}^{\text{min}}$. We use $R_{i,j}^{\text{min}}$ to denote the distance between sites i and j in this geometry. Furthermore, the linear term in n_i^k in the exponential in Eq. 17c has the same structure as the global detuning term in the Rydberg Hamiltonian (see Eq. 3), we therefore obtain 17d by making the identification

$$\Delta_g = -(V^{\alpha_v} + \Delta\mu^{\alpha_v}), \quad \Delta\mu^{\alpha_v} \equiv \frac{\Delta\mu}{\alpha_v}. \quad (18)$$

Here, $\Delta\mu^{\alpha_v}$ is the rescaled chemical potential, which plays a role analogous to V^{α_v} in enforcing a consistent overall energy rescaling. By comparing Eq. 17d and Eq. 17a, we conclude that the partition function Ξ sampled by the annealer at the effective sampling temperature T , global detuning Δ_g , and minimum interatomic spacing $R_{i,j}^{\text{min}}$ corresponds to the partition function of the material evaluated at the rescaled temperature

$$T' = T\alpha_v, \quad (19)$$

where α_v is given in Eq. 14.

Eqs. 14, 15, 18 and 19 define the mapping to implement the nitrogen-doped graphene model on the Rydberg-atom quantum hardware. Under this mapping, desirable energy scales, typically obtained from DFT calculations, that are inaccessible to the hardware become accessible due to a uniform rescaling, so that configurations that would be thermally populated in the physical system at temperature T' correspond to those populated in the hardware at an effective temperature T . This rescaling also modifies how we interpret the detuning. Per Eq. 18, we can explore a chemical potential range for the nitrogen-doped graphene model by varying the detuning $\Delta_g \in [-\Delta_g^{\max}, \Delta_g^{\max}]$. Within this interval, $\Delta_g = 0$ maps to $\Delta\mu = -V^{\text{DFT}}$, as shown in the center of the bottom panel of Fig. 2. Because of the rescaling, the annealer effectively samples the chemical potential of the nitrogen-doped graphene model within the range $\Delta\mu \in [-V^{\text{DFT}} - \alpha_v \Delta_g^{\max}, -V^{\text{DFT}} + \alpha_v \Delta_g^{\max}]$. Since $\alpha_v \approx 236.69$, the range of $\Delta\mu$ is two orders of magnitude larger than the energy scale of the hardware, as schematically illustrated in the bottom panel of Fig. 2. Rescaling is a critical step in our mapping, and any detuning value applied on the hardware, Δ_g , must therefore be multiplied by α_v to recover the corresponding effective chemical potential in the DFT-derived energies. In other words, the annealer samples the distribution associated with $\Delta\mu^{\alpha_v}$, not the original $\Delta\mu$. This distinction is crucial when comparing thermodynamic averages to classical calculations obtained, for example, from an exhaustive search or an unbiased Monte Carlo approach (Sections 2.4 and 2.5), or when benchmarking against experimental data.

2.4 Benchmarking the Quantum Annealing against an Exhaustive Search

In this section, we benchmark the mapping of the doped graphene system to the Rydberg atom hardware introduced in Section 2.3. Specifically, we estimate the effective sampling temperature of the Rydberg-atom system, a free parameter in the mapping, by running a small instance on the QPU and comparing the resulting average nitrogen concentration against that obtained classically through an exhaustive search. For this benchmark, we use the 28-site system depicted in Fig. 1 panel **b** and map it to a Rydberg-atom geometry with nearest-neighbour spacing fixed to the hardware minimum $R_{\text{NN}}^{\min} = 4\mu\text{m}$. We then execute the annealing protocol at ten values of Δ_g in $[-\frac{1}{2}\Delta_g^{\max}, \Delta_g^{\max}]$. The details of the annealing schedules are reported in the Methods section. At the end of the annealing, we measure the Rydberg occupation (see Section 2.1) and calculate the average concentration of nitrogen atoms as:

$$\overline{[N]}^{\text{qa}}(\Delta_g) = \frac{1}{N_{\text{qa}}} \sum_{s=1}^{N_{\text{qa}}} \|\mathbf{n}_s\|_1, \quad (20)$$

where $\overline{[N]}^{\text{qa}}(\Delta_g)$ denotes the average nitrogen concentration obtained at the value of Δ_g , N_{qa} is the number of times the quantum annealing was performed, \mathbf{n}_s is the binary vector returned by the QPU for sample s , and $\|\mathbf{n}_s\|_1$ denotes its ℓ^1 -norm (i.e., the Hamming weight, or the number of ones in the vector). Since nitrogen sites

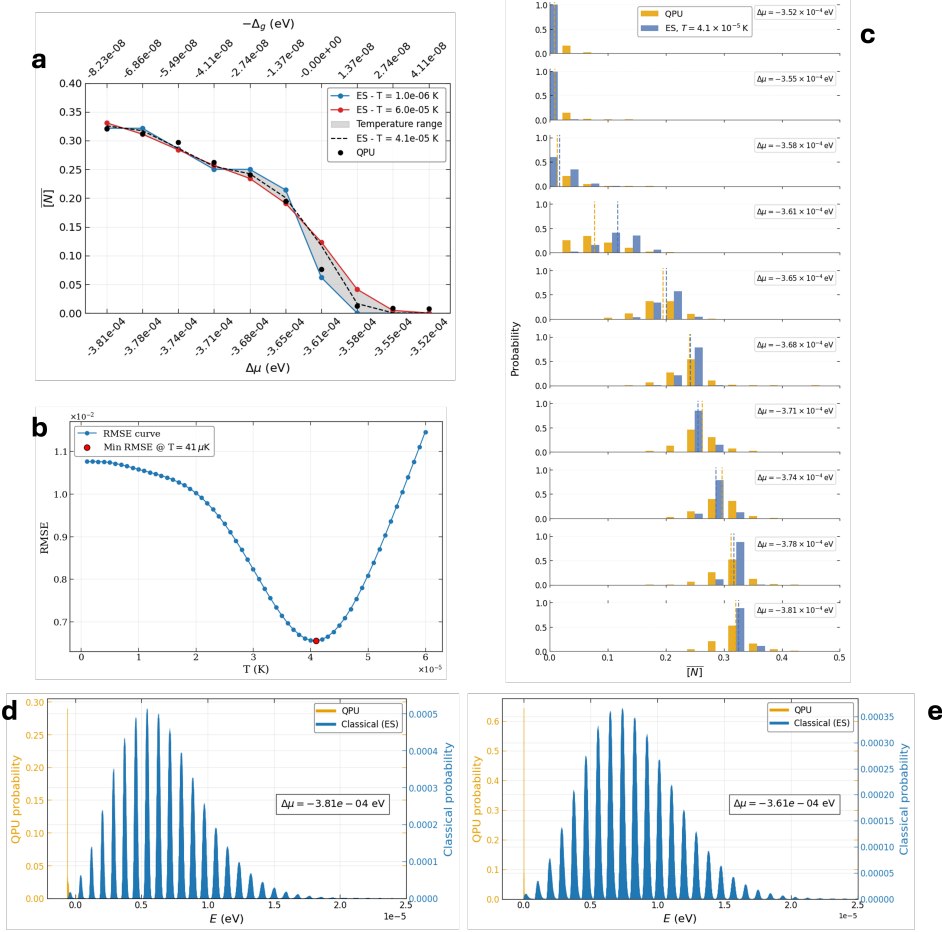


Fig. 3 QPU and exhaustive search data for the 28-site structure shown in Fig. 1b. Panel a reports the average nitrogen concentration as a function of $\Delta\mu$ (bottom x-axis) and Δ_g (top x-axis). Black dots indicate QPU data obtained at $R_{\text{NN}} = 4\mu\text{m}$. Blue and red curves correspond to exhaustive search results at $T = 1\mu\text{K}$ and $T = 60\mu\text{K}$, respectively, with the grey shaded area marking the range between these two temperatures. The dashed black line shows the result at $T = 41\mu\text{K}$, which minimises the RMSE with respect to the QPU data, as highlighted by the red dot in panel b. Each subplot in panel c corresponds to a different value of the chemical potential and displays the distribution of nitrogen concentration. The orange and blue dashed vertical lines mark the average concentration obtained from the QPU and from the exhaustive search at $T = 41\mu\text{K}$, respectively. Solid bars of the same colours illustrate the spread of concentrations around these mean values. Panels d and e display the number of states explored by the annealer (orange line) and by the exhaustive search (blue line) for the distribution at $\Delta\mu = -3.81 \times 10^{-4} \text{ eV}$ and $\Delta\mu = -3.61 \times 10^{-4} \text{ eV}$, respectively.

are mapped to 1 and Δ_g maps to the chemical potential of the doped graphene, we interpret $\langle N \rangle^{\text{qa}}(\Delta_g)$ as the average nitrogen concentration, which is a function of the chemical potential, obtained from the QPU. These are shown as black dots, in panel a of Fig. 3.

As described in Section 2.3, the QPU-estimated average nitrogen concentration corresponds to that of the doped graphene at a certain rescaled temperature. To determine that, we compare $\overline{[N]}^{\text{qa}}(\Delta_g)$ against the exact equilibrium prediction from the exhaustive search over the 28-site model across the same set of chemical potentials, and fit for the temperature that best matches the QPU data. Specifically, we calculate the average composition by performing an exhaustive search on the whole set of possible configurations containing between zero and twenty-eight nitrogen atoms. In this simulation, the energy of each configuration is calculated as:

$$E_k^{\text{Ry}} = \sum_i \Delta_g n_i^k + \sum_{i>j} \frac{C_6}{R_{i,j}^{\min}} n_i^k n_j^k, \quad (21)$$

which is the Rydberg energy (see Eq. 2 and Eq. 3) at the end of the annealing. The average nitrogen composition $\overline{[N]}^{\text{es}}(\Delta_g)$ obtained from the exhaustive search at global detuning Δ_g is determined by using:

$$\overline{[N]}^{\text{es}}(\Delta_g) = \sum_k p_k \|\mathbf{n}_k\|_1, \quad (22)$$

where \mathbf{n}_k is the binary vector mapping of structure k and the probability p_k of observing structure k is calculated classically as:

$$p_k = \frac{\exp \frac{-E_k^{\text{Ry}}}{k_B T}}{\sum_k \exp \frac{-E_k^{\text{Ry}}}{k_B T}}. \quad (23)$$

Here T is the effective sampling temperature of the annealer (see Eq. 19). Inspired by the hardware temperature being in the micro Kelvin regime, we sampled sixty temperatures from 1×10^{-6} K to 6×10^{-5} K. The resulting values are reported in Fig. 3 panel **a**. Here we plot the $\overline{[N]}^{\text{es}}(\Delta_g)$ for the minimum (blue line) and maximum (red line) temperatures sampled and shade the interval between the two (grey area). To identify the effective sampling temperature, we calculated the root mean squared error (RMSE) between each of the curves obtained at the temperatures we sampled and the QPU data (Fig. 3 panel **b**). We find the best fit (RMSE=6.55×10⁻³) to be at $T=41$ μK, and the $\overline{[N]}^{\text{es}}$ at this temperature is plotted as a dashed line in Fig. 3a. After extracting the annealer's effective sampling temperature from the average nitrogen concentration, we further validate the mapping by comparing the full distribution of the nitrogen concentration measured on the QPU with the corresponding classical predictions. For this, we calculate the energy of the complete set of configurations by using:

$$E_k^{\text{DFT}} = \sum_i (V^{\text{DFT}} + \Delta\mu) n_i^k + \sum_{ij} V_{i,j}^{\text{DFT}} n_i^k n_j^k. \quad (24)$$

From Eq. 18, the values of $\Delta\mu$ sampled range between $-V^{\text{DFT}} - \alpha_v \Delta_g^{\max}$ and $-V^{\text{DFT}} + \alpha_v \Delta_g^{\max}$. The average composition is then calculated using Eqs. 22 and 23 with E_k^{Ry} replaced by E_k^{DFT} and T replaced by the scaled temperature $T' = \alpha_v T$ defined in

Eq. 19. In Fig. 3c, each panel corresponds to a different value of $\Delta\mu$. The orange and blue bars show the nitrogen concentration spread around the average (dotted line) for the QPU and exhaustive search data at the rescaled temperature $T' = \alpha_v T = 9.71$ mK ($T = 41\mu\text{K}$), respectively. We obtain a Total Variation Distance (TVD) of 0.294 between the QPU and classical distributions, indicating good agreement: both the mean occupation and the spread of the distributions are well reproduced, showing that the QPU captures the expected thermodynamic behaviour. The largest deviation occurs at $\Delta\mu = -3.61 \times 10^{-4}$ eV ($\Delta_g = 0$), where the exhaustive search shows stronger temperature dependence due to the small energy differences involved.

An important result is displayed in panels d and e of Fig. 3, where we show the energy distributions of the configurations explored in the exhaustive search (blue line) and those sampled by the QPU (orange line) at $\Delta\mu = -3.81 \times 10^{-4}$ eV ($\Delta_g = -\Delta_g^{\max}$) and $\Delta\mu = -3.61 \times 10^{-4}$ eV ($\Delta_g = 0$), respectively. As the exhaustive search enumerates all configurations by construction, its distribution spans the full energy range of the system. In contrast, the QPU samples only the lowest-energy portion of the spectrum, reflecting its tendency to explore configurations close to the global minimum. For $\Delta\mu = -3.81 \times 10^{-4}$ eV, the majority of the states returned by the annealer have negative energies, confirming that the device predominantly identifies configurations that contain nitrogen atoms arranged to minimise pair interactions. At $\Delta\mu = -3.61 \times 10^{-4}$ eV, the lowest accessible energy is zero, and the sampled states indeed cluster around this value. In both panels, the left and right vertical axes use markedly different scales. This choice highlights that, while the exhaustive search populates the entire energy landscape, the QPU assigns almost all of its weight to the lowest-energy configurations permitted at the corresponding chemical potential.

2.5 Monte Carlo Benchmarking of Quantum Sampling

Since the benchmark in Sec. 2.4 shows good agreement between the annealing results and the exhaustive sampling for the smaller structure, we now turn to the larger system depicted in Fig. 1c. Because this structure contains 78 sites, the number of possible configurations within the composition range of interest exceeds 10^{21} , rendering exhaustive enumeration computationally intractable. We therefore employ unbiased Monte Carlo (UMC) sampling, generating a total of 10^8 random configurations. For each configuration, the energy is computed using Eq. 24, and the average concentration is evaluated according to Eq. 22, with probabilities defined in Eq. 23 using $T' = \alpha_v T$ where $T = 41\mu\text{K}$ as determined in Sec. 2.4. In Figure 4a, we compare the average nitrogen concentration from both the UMC and QPU as a function of Δ_g (top x-axis) and $\Delta\mu$ (bottom x-axis). We first consider the regime $\Delta_g > 0$. In this regime, a competition arises between the negative on-site term (see Eq. 3), which favours nitrogen incorporation, and the energy penalty associated with neighbouring nitrogen atoms. We find that, as the UMC sample size increases, configurations with higher nitrogen concentrations become more frequent. At the largest Δ_g value we benchmark, increasing the UMC sample size drives the average concentration toward the QPU result. This trend underscores the sampling challenge faced by UMC and highlights the efficiency of the QPU in reaching the relevant configurations at this detuning. We further find that the UMC estimates are systematically lower than the QPU results, with the

discrepancy shrinking as Δ_g decreases. An interesting point arises at $\Delta_g = 0$. In this case, the presence of a nitrogen atom provides no energetic advantage, while configurations containing interacting nitrogen pairs incur an energy penalty. As a result, the lowest achievable energy is zero, which occurs either when no nitrogen atoms are present or when they are placed sufficiently far apart to be considered non-interacting. This accentuates the trend already observed for $\Delta_g \gtrsim 0$, and regardless of the sample size, no increase in the calculated average composition is observed. Structures containing a larger number of non-interacting nitrogen atoms are rare within the full configurational space and are therefore difficult to capture using UMC, which samples configurations uniformly. In contrast, the quantum annealer explores only the low-lying energy landscape. Within this restricted region, the factorial growth of multiplicity makes high-nitrogen configurations more likely to appear, in accordance with the probabilities expected from a Boltzmann distribution obtained through exhaustive search.

To verify this interpretation, we examine the probability distribution as a function of nitrogen concentration for structures obtained at $\Delta_g = 0$, comparing the results from the QPU and from Monte Carlo (MC) sampling with 10^8 configurations, orange and blue bars, respectively, in Fig. 4c. In the UMC data, the highest probabilities correspond to structures containing no nitrogen atoms or a single nitrogen atom—both of which have zero energy—and the probability decreases steadily as the nitrogen content increases. Together, these configurations account for roughly 30% of the total probability, shifting the average nitrogen concentration towards lower values. However, these low-nitrogen structures have small multiplicities: there is only one pure graphene configuration and 78 distinct single-nitrogen configurations. In contrast, the QPU shows the highest probabilities for configurations containing two and three nitrogen atoms, which have multiplicities of 3003 and 76,076, respectively. Although many of these configurations are energetically penalised due to close nitrogen–nitrogen interactions, the QPU efficiently identifies the subset corresponding to zero energy. This ability to efficiently isolate the physically relevant, low-energy subset is one of the central results of our analysis. The combined probability of observing two- and three-nitrogen configurations exceeds 70%. As the nitrogen content increases beyond four atoms, the number of possible configurations grows factorially; however, only a small fraction is energetically favourable and is therefore rarely returned by the QPU.

This comparison highlights a fundamental difference between the two approaches: the MC method samples configurations uniformly across the entire configurational space, whereas the QPU effectively samples according to a Boltzmann-like distribution, concentrating probability on low-energy and high-multiplicity states. This contrast is illustrated in Fig. 4b, which shows the energy distributions obtained from the UMC analysis at $\Delta\mu = 0$ (blue line) and from the QPU (orange line). For clarity, both distributions are shown with truncated y -axes, as the dominant peak at $E = 0$ would otherwise obscure the remaining features. In addition, the vertical scale of the QPU distribution is an order of magnitude larger than that of the classical one; the corresponding peak heights are explicitly reported in the figure. Only a small fraction of the MC-generated configurations, approximately 0.073 of the total, have zero energy, while the remaining structures are broadly distributed across the accessible energy range. In

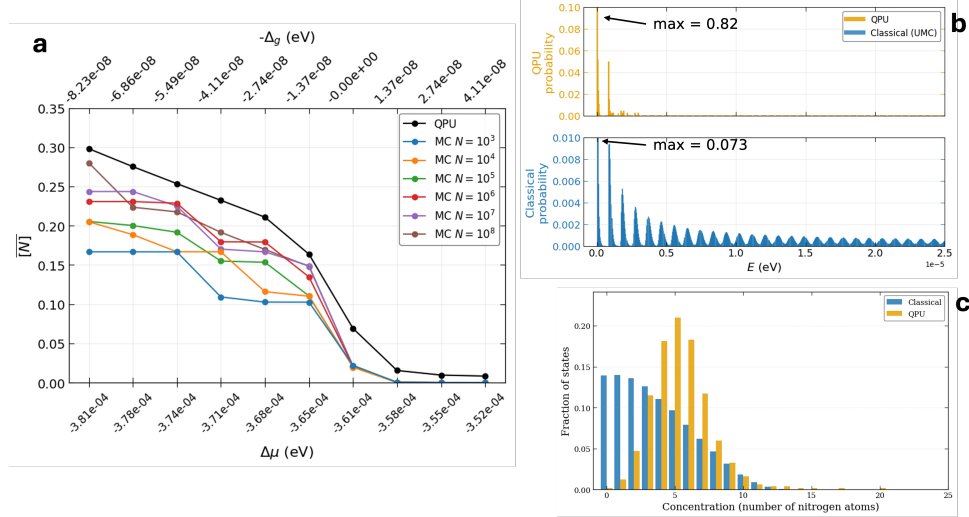


Fig. 4 QPU and Unbiased Monte Carlo (UMC) data for the 78-site structure shown in Fig. 1c. Panel a shows the average nitrogen concentration as a function of $\Delta\mu$ (bottom x-axis) and $-\Delta_g$ (top x-axis). Black dots and lines indicate QPU data obtained at $R_{\text{NN}} = 4 \mu\text{m}$, while coloured curves correspond to UMC results at $T = 41 \mu\text{K}$ for increasing sample sizes. Panel b compares the number of states explored by the annealer (orange line) and by the UMC (blue line) for $\Delta_g = 0 \text{ eV}$. Note that the y-axes have different orders of magnitude. Panel c shows the fraction of states per nitrogen concentration explored by the QPU (orange bars) and by the UMC (blue bars) at $\Delta_g = 0 \text{ eV}$.

contrast, the QPU output is sharply localised at low energies: about 0.82 of the configurations returned by the annealer lie exactly at $E = 0$, with a secondary, much smaller peak around $E = 1 \times 10^{-6} \text{ eV}$. This pronounced accumulation of probability at the lowest energies confirms that the QPU preferentially samples energetically favourable configurations, consistent with Boltzmann statistics and the expected thermodynamic behaviour. If we were to do an exhaustive search of all possible configurations, we would expect to recover the quantum hardware data as we did for the 28-atom system described in Section 2.4.

2.6 Tuning the Effective Temperature through Atomic Spacing

In Sec. 2.4 and 2.5, we focussed on how the average nitrogen concentration depends on the chemical potential. To investigate how it depends on temperature, we use the fact that the effective temperature in the mapped doped-graphene model can be tuned by varying the nearest-neighbour spacing in the Rydberg array. As shown in Eq. 19, the simulated temperature of the doped-graphene model is $T' = T \alpha_v$ where $\alpha_v = (R_{\text{NN}}/R_{\text{NN}}^{\text{DFT}})^6$. In the previous experiments, we fixed $R_{\text{NN}} = R_{\text{NN}}^{\text{min}}$, the minimum separation supported on the QPU. Here, we increase the distance between nearest neighbours to simulate different effective temperatures. In Fig. 5a, we report the nitrogen concentration distributions obtained for nearest-neighbour separations of $R_{\text{NN}} = 4 \mu\text{m}$, $4.5 \mu\text{m}$, and $5 \mu\text{m}$, corresponding to effective temperatures of $9.7 \times 10^{-3} \text{ K}$, $1.9 \times 10^{-2} \text{ K}$, and $3.6 \times 10^{-2} \text{ K}$, respectively. These results illustrate how

increasing the interatomic spacing on the hardware provides direct control over the effective sampling temperature.

As discussed above and formalised in Eq. 18, changing the interatomic distance also modifies the mapping between the global detuning Δ_g and the corresponding chemical potential $\Delta\mu$. As a result, the three curves in Fig. 5a do not span the same intervals of $\Delta\mu$. This effect is shown explicitly in Fig. 5b, where we plot $\Delta\mu$ as a function of Δ_g for the three interatomic separations. Increasing R_{NN} broadens the range of chemical potentials accessed for the same global detuning window.

For $R_{NN} = 5\text{ }\mu\text{m}$, the nitrogen concentration reaches a plateau at large negative values of $\Delta\mu$. In this regime, the configurations returned by the annealer correspond to structures that maximise nitrogen incorporation while avoiding nearest-neighbour nitrogen pairs. An example of such a configuration is shown in the inset of Fig. 5a. At this separation, the nearest-neighbour interaction energy between two simultaneously excited atoms is $2.28 \times 10^{-7}\text{ eV}$, which exceeds the maximum detuning available on the current QuEra device. Consequently, within the experimentally accessible range of Δ_g , configurations containing adjacent nitrogen atoms are suppressed for all interatomic distances considered here. We therefore expect that access to larger detuning values would enable sampling of configurations with higher nitrogen concentrations.

This result is particularly significant: in addition to demonstrating that the laser detuning in the quantum annealer can be directly mapped onto the chemical potential in the material, we show that Boltzmann-like distributions at different effective temperatures can be realised simply by tuning the interatomic distance in the hardware. This establishes a direct and experimentally accessible means of multivariate thermodynamic control within the quantum annealer.

3 Conclusions

In this work, we presented a workflow for mapping the DFT-derived energetics of nitrogen-doped graphene onto a Rydberg Hamiltonian, enabling quantum annealing on the QuEra Aquila hardware. The mapping expresses the formation energies in terms of an on-site term (implemented through the global detuning) and pairwise van der Waals interactions encoded through the programmable interatomic separations of the neutral-atom array.

A central contribution of this paper is the introduction of a rescaling factor, α_v , which takes into account the constraints of the hardware while preserving the thermodynamic structure of the problem. We showed analytically that this rescaling transforms the physical temperature to an effective annealing temperature following $T' = \alpha_v T$, ensuring that Boltzmann distributions are maintained even when the hardware cannot realise the exact DFT-derived interaction strengths.

The validity of the approach was demonstrated first on a 28-site graphene nanoflake through exhaustive enumeration, and subsequently on a 78-site system using unbiased Monte Carlo sampling, where the quantum annealer reproduced the expected thermodynamic behaviour despite the large configuration space. In addition, we showed that different effective temperatures can be realised experimentally by tuning the interatomic separation in the hardware, providing a direct means of thermodynamic control.

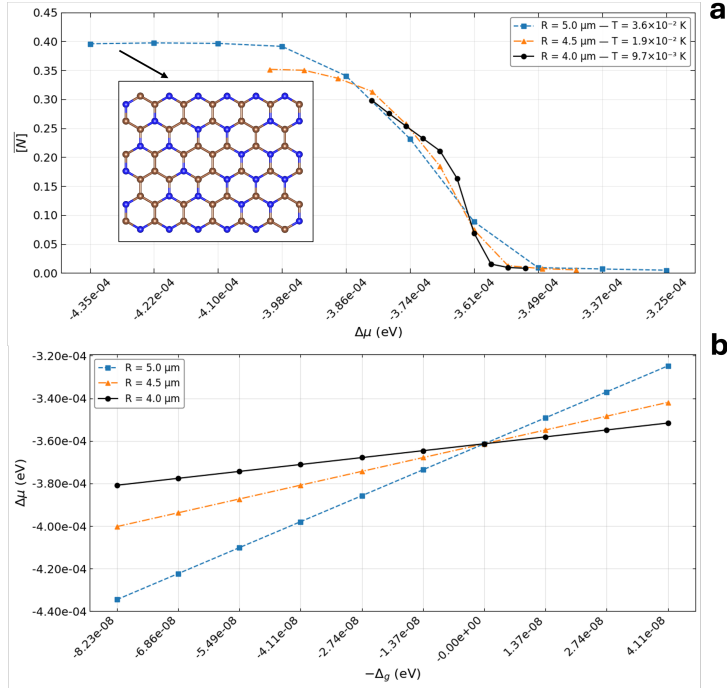


Fig. 5 Panel **a** shows the average nitrogen concentration in the 78-site graphene structure depicted in Fig. 1c as a function of the chemical potential $\Delta\mu$ at different interatomic distances in the hardware. The inset in this panel shows an example of structure returned by the annealer in the plateau region of the $R_{\text{NN}} = 5 \mu\text{m}$ (blue) line. Panel **b** displays how the chemical potential varies as a function of the global detuning Δ_g for the three interatomic separations obtained according to Eq. 18

4 Methods

4.1 Materials and DFT Calculation Details

Density functional theory (DFT) calculations for nitrogen-doped graphene were performed using the CRYSTAL23 code [23], which constructs crystalline orbitals from localised Gaussian basis functions. The exchange–correlation functional was treated within the PBE approximation [21], employing the revised pob-TZVP basis set [22], which includes polarisation functions for all elements.

The truncation of the Coulomb and exchange lattice series in CRYSTAL23 is governed by five thresholds, set to 8 (T1–T4) and 16 (T5). The self-consistent field (SCF) convergence criteria were 10^{-8} Hartree for total energy and 10^{-6} Hartree for structural relaxation. Reciprocal-space integration employed a Pack–Monkhorst grid centred at the Γ point, with shrinking factors of 6 and 12 for geometry optimisation and energy evaluation, respectively.

The graphene supercell used in these calculations contains 78 atomic sites (Fig. 1a). This cell was selected because it naturally accommodates the nanoflake structure

shown in Fig. 1c. Nitrogen dopants were introduced in concentrations ranging from one to ten atoms per cell, corresponding to 1.28%–12.8% nitrogen.

For the DFT dataset, we begin by generating configurations at random while enforcing that no two structures are related by the symmetries of the pristine graphene supercell. From this pool of symmetry-inequivalent configurations (SICs), we select a subset of size $N_{\text{train}}^{\text{SIC}}$ for explicit DFT evaluation. Each chosen SIC is relaxed at constant pressure, and its energy is then assigned to all symmetry-equivalent configurations (SECs) obtained by applying the space group operations of the underlying graphene lattice. In this way, a set of $N_{\text{train}}^{\text{SEC}}$ labelled structures is generated and used to fit the Rydberg Hamiltonian parameters. The same symmetry-based expansion is used for the test set. This symmetry-aware workflow allows us to construct a substantially larger training dataset than would be possible from direct DFT calculations alone.

Formation energies were referenced to molecular nitrogen and pristine graphene, ensuring that the energy of pure graphene is set to zero. Because CRYSTAL23 employs localised basis sets, the graphene calculations are periodic in two dimensions, while those for the nitrogen molecule are treated as zero-dimensional, without the need for vacuum separation.

The energies discussed above were calculated for a two-dimensional periodic layer of graphene, as illustrated in Fig. 1a. This approach simplifies the mapping of the DFT-derived energies onto the Rydberg Hamiltonian. However, in the annealing experiments we employ finite, non-periodic nanoflakes, shown in Fig. 1b and 1c. If the energies had been calculated directly for these non-periodic structures, slight variations would have appeared in the on-site energies and two-body interactions of atoms located at the edges, as these atoms have only two nearest neighbours instead of three, unlike those in the centre of the cell. In principle, the resulting variations in on-site energies could be compensated by using site-dependent local detuning. However, the corresponding differences in $V_{i,j}$ would lead to modified atomic positions that cannot be realised on the hardware, given the geometric constraints discussed in the main text. For this reason, we extract a portion of the periodic graphene layer and treat it as representative of the bulk material.

This approximation has a clear physical consequence: nitrogen atoms tend to occupy boundary sites more frequently than they would in a fully periodic model, where atoms at opposite edges are nearest neighbours. The energetic implication is that, in the non-periodic case, the energy associated with two distant nitrogen atoms is $2V^{\text{DFT}}$, whereas in the periodic system it is $2V^{\text{DFT}} + V_{\text{NN}}^{\text{DFT}}$. As a result, configurations with nitrogen atoms at the boundaries are slightly overrepresented during thermodynamic sampling compared with those in the centre of the flake. Nevertheless, the number of such configurations is small relative to the total, and their contribution becomes negligible as the system size increases.

Unlike D-Wave annealers [8, 25], the QuEra architecture does not natively support periodic boundary conditions. In principle, opposite sides of the cell could be connected through additional “gadgets,” as proposed in Ref. [26], but this approach would introduce substantial hardware overhead. For this reason, we did not pursue this route in the present work. However, periodic boundary conditions could be achieved, in principle, with a reconfigurable atom array.

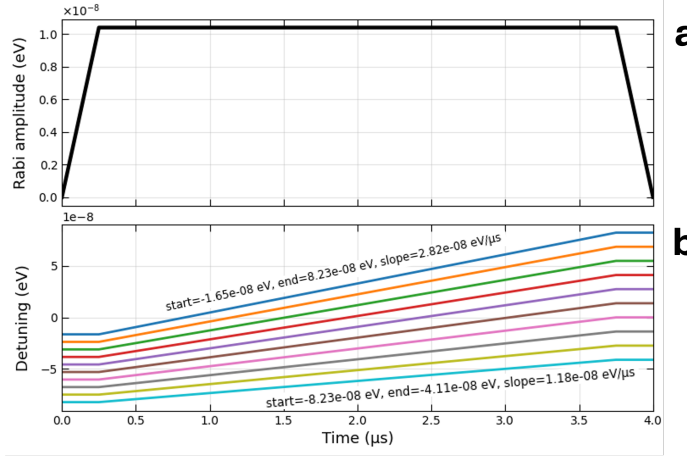


Fig. 6 Laser energies used in the experiments reported in this work. Panel **a** depicts the Rabi amplitude values throughout the annealing. Panel **b** shows the detuning values variations during the annealing for the ten different values of final Δ_g used in the Results sections.

4.2 Quantum Annealing Details

Quantum annealing was performed on the QuEra Aquila [16] device. These employ Rb-87 atoms are held and cooled to microkelvin temperatures by laser beams inside a vacuum cell. Reconfigurable optical tweezers enable the arbitrary arrangements of up to 256 atoms. The annealing is carried out by lasers that excite the Rb-87 atoms to their Rydberg state where they interact with each other.

In our experiments, two types of laser pulses are applied during the annealing process, as illustrated in Fig. 6. Panel **a** of the figure shows the Rabi drive, which is kept identical across all experiments, while the **b** panel depicts the global detuning, whose slope varies depending on its final value. Ideally, the detuning profile should remain consistent between experiments; to achieve this, we implemented a piecewise-linear detuning scheme. Each detuning pulse was divided into three regions: an initial and a final hold, each spanning 6.25% of the total sequence duration, and a central 87.5% linear ramp connecting the starting and ending detuning values. The total pulse duration was fixed at $t = 4 \mu\text{s}$. The final detuning values were chosen to decrease linearly from $-8.23 \times 10^{-8} \text{ eV}$ to $4.11 \times 10^{-8} \text{ eV}$. The corresponding initial detuning values were clipped at the lower hardware limit of $8.23 \times 10^{-8} \text{ eV}$. This construction yields ramp rates between $2.82 \times 10^{-8} \text{ eV}/\mu\text{s}$ and $1.18 \times 10^{-8} \text{ eV}/\mu\text{s}$ while maintaining identical pulse shapes and timing across all experiments. This method ensures moderate slope variation within the detuning window, preventing abrupt transitions while covering a large fraction of the available dynamic range. For each data point, the annealing protocol was executed 1000 times in order to obtain statistically meaningful thermodynamic averages. Prior to annealing, the rubidium atoms are arranged in the target geometry; however, due to experimental imperfections, not all sites are occupied in every run. To ensure consistency, we retain only those annealing outcomes corresponding to fully occupied initial configurations. Across all experiments reported in this work, the

fraction of runs with complete initial occupancy averaged 60.5%, with a standard deviation of 12.1%. The observed occupancy fraction ranged from a minimum of 40.6% to a maximum of 81.4%, depending on the experiment.

4.3 Phosphorous–Nitrogen Co-doping: Challenges for the Current Mapping

In this section, we briefly examine an extension of the nitrogen-doped graphene model in which a single phosphorous atom is introduced at a fixed lattice site. The system is described using the 78-site graphene cell shown in Fig. 1c, with the phosphorous atom placed at the centre of the structure and held fixed throughout the analysis. This case is included to illustrate the challenges that arise when additional chemical complexity is introduced, and to clarify the limitations of the current mapping strategy when applied to systems with strong, localised interactions.

For this problem we make one additional modelling assumption: we retain the two-body nitrogen–nitrogen interaction energy obtained in Eq. 5, and allow only the on-site energy of nitrogen to vary in order to capture its preference to sit closer or further from the phosphorous atom. To obtain this distance-dependent on-site term, a single nitrogen atom is placed, one site at a time, at each symmetry-inequivalent distance from the phosphorous atom. The resulting eighteen structures are relaxed and their energies computed using DFT. The on-site potential at each distance is then defined relative to a reference configuration in which the nitrogen atom is placed at the maximum separation allowed by the cell (9.34 Å), where the interaction with phosphorous is considered to be negligible. The resulting distance-dependent on-site energies are shown in Fig. 7. As expected, nitrogen strongly favours occupying a site adjacent to phosphorous (energy gain of -1.11 eV). This behaviour reflects the distinct atomic radius and electronegativity of the two dopants. Phosphorus has a significantly larger covalent radius than carbon and nitrogen, leading to local lattice distortion when incorporated into the graphene network. Nitrogen, by contrast, is smaller and more electronegative, and preferentially stabilises regions of high local strain and charge redistribution. When placed adjacent to phosphorus, nitrogen partially compensates the local structural and electronic perturbation induced by the larger dopant, resulting in a net stabilisation of the local bonding environment and a lower formation energy.

This chemical preference introduces the first of two challenges when mapping this system to the quantum annealer. The energy scale associated with the nitrogen–phosphorous interaction is approximately four orders of magnitude larger than the on-site term V^{DFT} extracted from the nitrogen–nitrogen problem. Since the local detuning on the hardware has the same energy scale as the global detuning, even after applying the rescaling procedure introduced above, the local term would dominate and suppress any global-detuning driven sampling of compositions. The second challenge is that the effective interactions are no longer strictly two-body. The strong stabilisation of a nitrogen atom placed next to phosphorus is specific to the first dopant and arises from a combination of local lattice relaxation due to the larger atomic radius of phosphorus and the electronegativity contrast between the two species. Once one nitrogen atom occupies the site adjacent to phosphorous, the energy gain associated with placing a second nitrogen nearby decreases to -6.35×10^{-1} eV (about

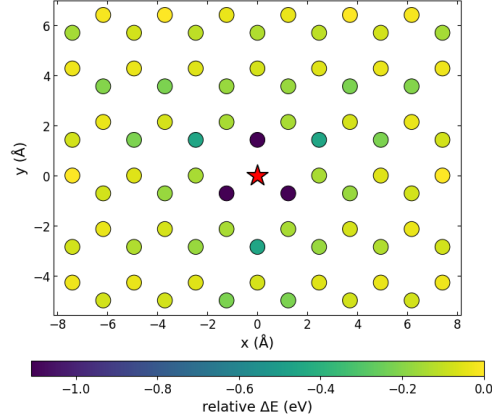


Fig. 7 Graphene structure containing 78 sites used to construct the energy model for phosphorous-doped graphene. The red star marks the position of the phosphorous atom. Circles denote the carbon sites, and the heat-map colour scale indicates the energy associated with placing a nitrogen atom at each site relative to placing it at the maximum separation, where the nitrogen–phosphorous interaction is negligible.

57% smaller), and to -2.86×10^{-1} eV (26% smaller) when a third is added. Thus, the energetics depend on the number of nitrogen atoms already present in the local environment. These higher-order many-body effects cannot be captured by a purely two-body Hamiltonian. In principle, this behaviour could be approximated by averaging the distance-dependent interaction energies, but such an approach would obscure the many-body nature of the problem. A more rigorous treatment would require a Hamiltonian capable of representing higher-order interactions, such as a Higher-Order Unconstrained Binary Optimisation (HUBO) model. While current Rydberg-atom hardware natively supports only two-body interactions, future architectures incorporating multi-body couplings may enable an exact mapping of this class of chemically complex systems.

References

- [1] Purton, J.A., Lavrentiev, M.Y., Allan, N.L.: Monte carlo simulation of gan/aln and aln/inn mixtures. *Materials Chemistry and Physics* **105**(2), 179–184 (2007) <https://doi.org/10.1016/j.matchemphys.2007.04.024>
- [2] Mohn, C.E., Kob, W.: Predicting complex mineral structures using genetic algorithms. *Journal of Physics: Condensed Matter* **27**(42), 425201 (2015) <https://doi.org/10.1088/0953-8984/27/42/425201>
- [3] and, C.E.M.: Predicting cation ordering in mgal2o4 using genetic algorithms and density functional theory. *Materials and Manufacturing Processes* **33**(2), 174–179 (2018) <https://doi.org/10.1080/10426914.2017.1303153> <https://doi.org/10.1080/10426914.2017.1303153>
- [4] Allan, N.L., Thomas, L., Hart, J.N., Freeman, C.L., Mohn, C.E.: Calcite–magnesite solid solutions: using genetic algorithms to understand non-ideality. *Physics and Chemistry of Minerals* **46**(2), 193–202 (2019) <https://doi.org/10.1007/s00269-018-0997-3>
- [5] Gusev, V.V., Adamson, D., Deligkas, A., Antypov, D., Collins, C.M., Krysta, P., Potapov, I., Darling, G.R., Dyer, M.S., Spirakis, P., *et al.*: Optimality guarantees for crystal structure prediction. *Nature* **619**(7968), 68–72 (2023)
- [6] Choubisa, H., Abed, J., Mendoza, D., Matsumura, H., Sugimura, M., Yao, Z., Wang, Z., Sutherland, B.R., Aspuru-Guzik, A., Sargent, E.H.: Accelerated chemical space search using a quantum-inspired cluster expansion approach. *Matter* **6**(2), 605–625 (2023) <https://doi.org/10.1016/j.matt.2022.11.031>
- [7] Binninger, T., Ting, Y.-Y., Köster, K., Bruch, N., Kaghazchi, P., Kowalski, P.M., Eikerling, M.H.: Simulating charging characteristics of lithium iron phosphate by electro-ionic optimization on a quantum annealer. *Phys. Rev. B* **112**, 174118 (2025) <https://doi.org/10.1103/cpgy-fpvb>
- [8] Camino, B., Buckeridge, J., Chancellor, N., Catlow, C.R.A., Ferrari, A.M., Warburton, P.A., Sokol, A.A., Woodley, S.M.: Exploring the thermodynamics of disordered materials with quantum computing. *Science Advances* **11**(23), 7156 (2025) <https://doi.org/10.1126/sciadv.adt7156> <https://www.science.org/doi/pdf/10.1126/sciadv.adt7156>
- [9] Kochenberger, G.A., Glover, F., Wang, H.: In: Pardalos, P.M., Du, D.-Z., Thai, M.T. (eds.) QUBO: Quadratic Unconstrained Binary Optimization Problem, pp. 1–26. Springer, New York, NY (2025). https://doi.org/10.1007/978-1-4614-6624-6_15-1 . https://doi.org/10.1007/978-1-4614-6624-6_15-1
- [10] Lucas, A.: Ising formulations of many NP problems. *Frontiers in Physics* **2**, 5 (2014) <https://doi.org/10.3389/fphy.2014.00005>

- [11] D-Wave systems. <https://www.dwavesys.com/> <https://www.dwavesys.com/>
- [12] Browaeys, A., Lahaye, T.: Many-body physics with individually controlled rydberg atoms. *Nature Physics* **16**(2), 132–142 (2020) <https://doi.org/10.1038/s41567-019-0733-z>
- [13] Henriet, L., Beguin, L., Signoles, A., Lahaye, T., Browaeys, A., Reymond, G.-O., Jurczak, C.: Quantum computing with neutral atoms. *Quantum* **4**, 327 (2020) <https://doi.org/10.22331/q-2020-09-21-327>
- [14] Bluvstein, D., Levine, H., Semeghini, G., Wang, T.T., Ebadi, S., Kalinowski, M., Keesling, A., Maskara, N., Pichler, H., Greiner, M., Vuletić, V., Lukin, M.D.: A quantum processor based on coherent transport of entangled atom arrays. *Nature* **604**(7906), 451–456 (2022) <https://doi.org/10.1038/s41586-022-04592-6>
- [15] Wintersperger, K., Dang, H.-L., Capecci, G., Krinner, S., Scheuer, J., Fedorov, A., Barredo, D., Browaeys, A., Kuhr, S., Monz, T., Schaetz, T., Blatt, R., Bloch, I.: Neutral atom quantum computing hardware: Performance and end-user perspective. *EPJ Quantum Technology* **10**, 32 (2023) <https://doi.org/10.1140/epjqt/s40507-023-00190-1>
- [16] Wurtz, J., Bylinskii, A., Braverman, B., Amato-Grill, J., Cantu, S.H., Huber, F., Lukin, A., Liu, F., Weinberg, P., Long, J., Wang, S.-T., Gemelke, N., Keesling, A.: Aquila: Quera’s 256-qubit neutral-atom quantum computer (2023) [arXiv:2306.11727](https://arxiv.org/abs/2306.11727) [quant-ph]
- [17] Zhao, M., Singh, M., Singh, A., Thoreen, H., DeAngelo, R.J., Dominguez, D., Leenheer, A., Peyskens, F., Lukin, A., Englund, D., Eichenfield, M., Gemelke, N., Wan, N.H.: An integrated photonics platform for high-speed, ultrahigh-extinction, many-channel quantum control (2025). <https://arxiv.org/abs/2508.09920>
- [18] Hohenberg, P., Kohn, W.: Inhomogeneous electron gas. *Physical Review* **136**(3B), 864–871 (1964) <https://doi.org/10.1103/PhysRev.136.B864>
- [19] Kohn, W., Sham, L.J.: Self-consistent equations including exchange and correlation effects. *Physical Review* **140**(A4), 1133–1138 (1965) <https://doi.org/10.1103/PhysRev.140.A1133>
- [20] Barredo, D., Lienhard, V., Léséleuc, S., Lahaye, T., Browaeys, A.: Synthetic three-dimensional atomic structures assembled atom by atom. *Nature* **561**(7721), 79–82 (2018) <https://doi.org/10.1038/s41586-018-0450-2>
- [21] Perdew, J.P., Burke, K., Ernzerhof, M.: Generalized gradient approximation made simple. *Phys. Rev. Lett.* **77**, 3865–3868 (1996) <https://doi.org/10.1103/PhysRevLett.77.3865>
- [22] Vilela Oliveira, D., Laun, J., Peintinger, M.F., Bredow, T.: Bsse-correction

scheme for consistent gaussian basis sets of double- and triple-zeta valence with polarization quality for solid-state calculations. *Journal of Computational Chemistry* **40**(27), 2364–2376 (2019) <https://doi.org/10.1002/jcc.26013> <https://onlinelibrary.wiley.com/doi/pdf/10.1002/jcc.26013>

- [23] Erba, A., Desmarais, J.K., Casassa, S., Civalleri, B., Donà, L., Bush, I.J., Searle, B., Maschio, L., Edith-Daga, L., Cossard, A., Ribaldone, C., Ascrizzi, E., Marana, N.L., Flament, J.-P., Kirtman, B.: Crystal23: A program for computational solid state physics and chemistry. *Journal of Chemical Theory and Computation* **0**(0), (0) <https://doi.org/10.1021/acs.jctc.2c00958> <https://doi.org/10.1021/acs.jctc.2c00958>. PMID: 36502394
- [24] Camino, B., Lin, M.: Rydberg Atoms: The Final Notebook. https://github.com/cmc-ucl/rydberg_atoms/blob/main/The_final_nb.ipynb (2025)
- [25] Camino, B., Buckeridge, J., Warburton, P.A., Kendon, V., Woodley, S.M.: Quantum computing and materials science: A practical guide to applying quantum annealing to the configurational analysis of materials. *Journal of Applied Physics* **133**(22), 221102 (2023) <https://doi.org/10.1063/5.0151346> https://pubs.aip.org/aip/jap/article-pdf/doi/10.1063/5.0151346/19847991/221102_1_5.0151346.pdf
- [26] Nguyen, M.-T., Liu, J.-G., Wurtz, J., Lukin, M.D., Wang, S.-T., Pichler, H.: Quantum optimization with arbitrary connectivity using rydberg atom arrays. *PRX Quantum* **4**, 010316 (2023) <https://doi.org/10.1103/PRXQuantum.4.010316>